Rapid #: -9076006

A Controller Framework for Autonomous Drifting: Design, Stability, and Experimental Validation

Rami Y. Hindiyeh[1]
Dynamic Design Laboratory,
Department of Mechanical Engineering,
Stanford University,
Stanford, CA 94305
e-mail: hindiyeh@alumni.stanford.edu

J. Christian Gerdes
Associate Professor
Dynamic Design Laboratory,
Department of Mechanical Engineering,
Stanford University,
Stanford, CA 94305
e-mail: gerdes@stanford.edu

This paper presents the development of a controller for autonomous, steady-state cornering with rear tire saturation ("drifting") of a rear wheel drive vehicle. The controller is designed using a three-state vehicle model intended to balance simplicity and sufficient model fidelity. The model has unstable "drift equilibria" with large rear drive forces that induce deep rear tire saturation. The rear tire saturation at drift equilibria reduces vehicle stability but enables "steering" of the rear tire force through friction circle coupling of rear tire forces. This unique stability–controllability tradeoff is reflected in the controller design, through novel usage of the rear drive force for lateral control. An analytical stability guarantee is provided for the controller through a physically insightful invariant set around a desired drift equilibrium when operating in closed-loop. When implemented on a by-wire testbed, the controller achieves robust drifts on a surface with highly varying friction, suggesting that steady cornering with rear tire saturation can prove quite effective for vehicle trajectory control under uncertain conditions. [DOI: 10.1115/1.4027471]

1 Introduction

High-sideslip cornering represents an impressive feat of vehicle control undertaken by the world's most skilled drivers. Cornering in this fashion is quite dramatic because it is characterized by a large sideslip angle, which gives the angle between the vehicle's velocity vector at the center of gravity (CG) and its longitudinal axis. Simply speaking, this means that the vehicle corners while traveling noticeably "sideways" to some extent. From a vehicle dynamics perspective, high-sideslip cornering is intriguing because it involves deliberate, deep saturation of the rear tires, well beyond their limits of adhesion. Considering that typical, low-sideslip driving practices avoid rear tire saturation because of the potential for vehicle destabilization, high-sideslip cornering is obviously rather extreme in nature. And yet, it is prevalent in racing on dirt, gravel, and ice, all surfaces where friction is uncertain and can vary considerably.

The fact that some of the world's best drivers deliberately corner at high-sideslip with rear tire saturation in uncertain conditions suggests that there is much to be learned about vehicle control under such circumstances from their techniques. A fundamental exploration of the dynamics and control of high-sideslip maneuvers and cornering with rear tire saturation can provide physical insights into the characteristics of these maneuvers that make them useful in uncertain conditions. While this is certainly illuminating in understanding the role of cornering with saturated rear tires in competitive driving, it also has the potential to influence future development of vehicle safety and driver assistance systems, where robust performance under a broad range of conditions is obviously desirable.

There are several different types of maneuvers within the broader category of cornering with rear tire saturation. Many of these maneuvers, such as the "pendulum turns" used in rally racing, involve transient high-sideslip motion and saturation of the rear tires. A fair amount of prior research has focused on these transient maneuvers, including work exploring optimality of these maneuvers on low friction surfaces under a variety of conditions.

Velenis and Tsiotras produced transient high-sideslip maneuvers in simulation when maximizing corner exit velocity [1] or minimizing time through a corner with special constraints, such as a limited distance to re-orient the vehicle or a specific parameterization of the driver inputs [2]. The research presented in this paper instead focuses on steady-state cornering with rear tire saturation, known in automotive circles as "drifting." This work is divided into two parts, with the first exploring the dynamics of drifting as captured using a relatively simple vehicle model and the second building upon this understanding to develop a controller capable of drifting a vehicle autonomously.

Prior work has demonstrated that drifting is an unstable equilibrium condition of a rear wheel drive (RWD) vehicle model. The vehicle's rear tires are saturated at "drift equilibria," and these equilibria are typically characterized by countersteer and a high-sideslip angle. Interestingly, drift equilibria have been encountered across a wide range of model fidelities, from simple two-state models by Ono et al. [3] and Voser et al. [4] to high-fidelity models by Edelmann et al. [5] and Velenis et al. [6] that incorporate load transfer and relatively complex tire models.

Nonetheless, the models in prior work do not necessarily achieve an ideal balance between sufficient model fidelity and simplicity from a control design standpoint. Higher-fidelity models such as the ones in Refs. [5] and [6] capture both the lateral and longitudinal dynamics of the vehicle, but their added complexity reduces physical intuition and prevents the usage of simple analysis techniques, such as the phase portraits in Ref. [3]. The simple models in Refs. [3] and [4], on the other hand, retain physical intuition but do not include the longitudinal dynamics of the vehicle. This is problematic, as several results in literature show that a large rear longitudinal force, controlled in coordination with steering, is a critical component of drifting. This is apparent from the equilibrium analyses in Refs. [5] and [6]. It is also evident in examinations of experimental data from drivers drifting in Velenis et al. [6] and Abdulrahim [7].

This work seeks to bridge the gap between model fidelity and simplicity for control design with a three-state model that treats rear longitudinal force as a direct input. An equilibrium analysis with this model reveals the existence of equilibria possessing all the characteristics of drifting described above, while also confirming the necessity of a large rear drive force at such equilibria.

---

[1]Corresponding author.
Contributed by the Dynamic Systems Division of ASME for publication in the JOURNAL OF DYNAMIC SYSTEMS, MEASUREMENT, AND CONTROL. Manuscript received January 19, 2012; final manuscript received April 16, 2014; published online July 9, 2014. Assoc. Editor: Shankar Coimbatore Subramanian.

More importantly, this analysis facilitates a new way of looking at drifting from a control perspective, as a tradeoff of vehicle stability for enhanced controllability. To be specific, the analysis demonstrates that the rear tire saturation inherent to drifting reduces vehicle stability but enhances controllability by allowing "steering" of the rear tire using the rear longitudinal force. This concept plays a central role in the design of the controller for autonomous drifting in this work, and in particular the role of rear longitudinal force as a control input.

There are several instances of controllers for autonomous drifting in prior work, utilizing several different combinations of actuators. In Ref. [4], Voser et al. present a controller that uses front steering alone operating in parallel with a simple cruise control, but this controller suffers from disturbance rejection issues, including uncontrolled exits from drifting and into conventional cornering. Edelmann et al. [8] and Velenis et al. [6] present controllers that use both steering and rear longitudinal inputs for autonomous drifting. However, these controllers are designed using linearized models; in the case of Ref. [8], the authors acknowledge that the design can only tolerate moderate disturbances as a result. Velenis et al. have also published sliding mode control designs for autonomous drifting that utilize actuation not directly available to a human driver, such as independent control of front and rear wheel torques in Ref. [9]. While these additional actuator capabilities allow for added flexibility in control design, a controller utilizing such actuation cannot shed light upon how drifting is controlled by human drivers with the "standard" actuation available to them.

The controller in this work uses steering and rear drive force in coordination, leveraging the ability to "steer" the rear tire using the rear drive force directly in its design. Furthermore, the design has demonstrable stability characteristics, with a physically insightful invariant set calculated using simple Lyapunov techniques. Finally, and perhaps most importantly, the controller has been experimentally validated on a by-wire testbed under challenging test conditions. It achieves sustained, robust drifts in the presence of disturbances from significant friction variation, not only validating the control design but also bolstering the notion of using cornering with rear tire saturation to contend with uncertain conditions.

2 Vehicle Model

The controller design in this paper is based on the three-state bicycle model depicted in Fig. 1. In this model, the front and rear tires are lumped into a single tire at each axle, the vehicle's motion is planar, and the vehicle is RWD (no longitudinal force at the front tire). The model's motion is described in terms of a body-fixed coordinate system at the vehicle CG that conforms to the ISO 8855 standard.

The model states are sideslip β at the CG (based on lateral velocity U_y at the CG), yaw rate r (rotation rate normal to the plane), and longitudinal velocity U_x at the CG. The model inputs are the front steer angle δ and the rear drive force $F_{xR} > 0$. With the approximations $\cos \delta \approx 1$, $\beta \approx U_y/U_x$, and $\dot{\beta} \approx \dot{U}_y/U_x$, the governing equations for the model are

$$
\begin{aligned}
\dot{\beta} &= \frac{1}{mU_x}(F_{yF} + F_{yR}) - r \\
\dot{r} &= \frac{1}{I_z}(aF_{yF} - bF_{yR}) \\
\dot{U}_x &= \frac{1}{m}(F_{xR} - F_{yF}\sin\delta) + rU_x\beta
\end{aligned}
\tag{1}
$$

where m is the vehicle mass, I_z is the vehicle's yaw inertia, a is the distance from the vehicle CG to the front axle, b is the distance from the vehicle CG to the rear axle, F_{yF} is the front tire lateral force, and F_{yR} is the rear tire lateral force.

For the sideslip magnitudes considered in this work ($|\beta| \approx 20\,\text{deg}$), the small angle approximation on β introduces
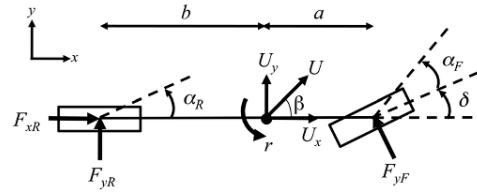

Fig. 1 Bicycle model of a RWD vehicle

approximately 4.3% of error relative to the actual value. Similarly, the small angle approximation on $\cos\delta$ introduces 8.6% of error or less relative to the actual value within the steering range of the test vehicle ($|\delta| \leq 23\,\text{deg}$). These errors are on the same order of magnitude (if not smaller) than the modeling errors caused by friction uncertainty when operating on a dirt or gravel surface.

The tire lateral forces F_{yF} and F_{yR} are calculated using a slightly modified version of the Fiala lateral tire force model [10]. The model is given in Eq. (2)

$$
\begin{aligned}
F_y &= \begin{cases} -C_\alpha z + \dfrac{C_\alpha^2}{3\xi\mu F_z}|z|z - \dfrac{C_\alpha^3}{27\xi^2\mu^2 F_z^2}z^3 & |z| < \tan\alpha_{\text{sl}} \\[2mm] -\xi\mu F_z \text{sgn}\,\alpha & |z| \geq \tan\alpha_{\text{sl}} \end{cases} \\[2mm]
z &= \tan\alpha \\[2mm]
\alpha_{\text{sl}} &= \arctan\frac{3\xi\mu F_z}{C_\alpha}
\end{aligned}
\tag{2}
$$

where C_α is the tire cornering stiffness, F_z is the normal load applied to the tire, α is the tire slip angle (a function of U_y, r and U_x), and μ is the friction coefficient between the tire and the ground. As detailed in Ref. [4], the tire parameters are identified from force curves for each axle as obtained during steady-state cornering. These empirical curves represent the effective lumped tire force at each axle and account for the effects of steady-state lateral weight transfer without including roll dynamics or weight transfer in the vehicle model explicitly.

The ξ in Eq. (2) is a derating factor ($0 \leq \xi \leq 1$) that accounts for a reduction in lateral force capacity when longitudinal force is applied. The rear tire derating factor ξ_R will vary depending upon the longitudinal force input F_{xR} to the rear tire and is readily calculated from Eq. (3)

$$
\xi_R = \frac{\sqrt{(\mu F_{zR})^2 - F_{xR}^2}}{\mu F_{zR}}
\tag{3}
$$

Equation (3) is a simple rearrangement of the "friction circle" equation for the rear tire, which dictates that the total force generated at the tire cannot exceed the total force available at the tire from friction. For the front tire, $\xi_F = 1$ since there is no drive force applied at the front tire. By treating lateral–longitudinal force coupling in this fashion, it is possible to treat longitudinal force as an input and eliminate the additional complexity of wheelspeed dynamics and a tire model that incorporates wheel slip.

The results presented in the remainder of this work have been obtained using the following parameter set for the model described above: $m = 1724\,\text{kg}$, $I_z = 1300\,\text{kg/m}^2$, $a = 1.35\,\text{m}$, $b = 1.15\,\text{m}$, $C_{\alpha F} = 120{,}000\,\text{N/rad}$, $C_{\alpha R} = 175{,}000\,\text{N/rad}$, and $\mu = 0.55$. This parameter set corresponds to the P1 by-wire test vehicle depicted in Fig. 2.

3 Equilibrium Analysis

The vehicle is in an equilibrium state when all state derivatives of the model are zero, e.g., $\dot{\beta} = \dot{r} = \dot{U}_x = 0$. Beginning with the vehicle state equations in Eq. (1), this results in the system of algebraic equations given in Eq. (4)
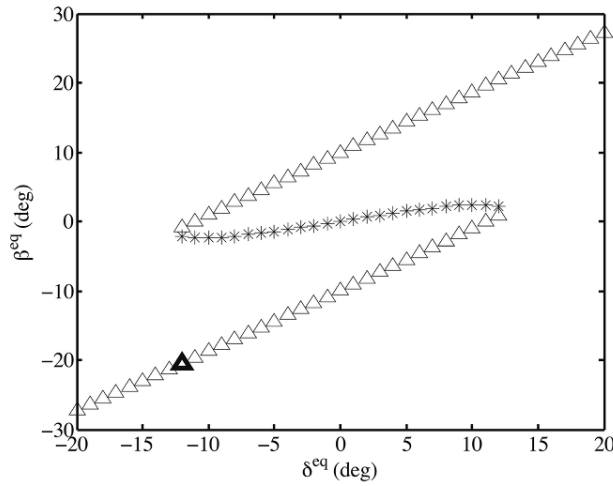
Fig. 2 P1, a by-wire test vehicle

Fig. 3 Equilibrium sideslip versus steer angle, $U_x = 8\,\text{m/s}$

Fig. 4 Equilibrium yaw rate versus steer angle, $U_x = 8\,\text{m/s}$
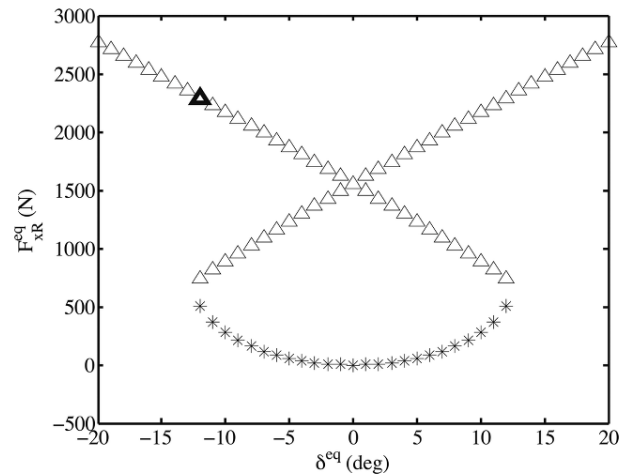
Fig. 5 Equilibrium rear longitudinal force versus steer angle, $U_x = 8\,\text{m/s}$

$$\frac{1}{mU_x^{\text{eq}}}\left(F_{y\text{F}}^{\text{eq}} + F_{y\text{R}}^{\text{eq}}\right) - r^{\text{eq}} = 0$$

$$\frac{1}{I_z}\left(aF_{y\text{F}}^{\text{eq}} - bF_{y\text{R}}^{\text{eq}}\right) = 0 \qquad (4)$$

$$\frac{1}{m}\left(F_{x\text{R}}^{\text{eq}} - F_{y\text{F}}^{\text{eq}}\sin\delta^{\text{eq}}\right) + r^{\text{eq}}U_x^{\text{eq}}\beta^{\text{eq}} = 0$$

where $F_{y\text{F}}^{\text{eq}}, F_{y\text{R}}^{\text{eq}}, F_{x\text{R}}^{\text{eq}}, \delta^{\text{eq}}, \beta^{\text{eq}}, r^{\text{eq}}$, and U_x^{eq} are the equilibrium values of the lateral tire forces, rear longitudinal tire force, steer angle, and vehicle states as defined previously. Since $F_{y\text{F}}^{\text{eq}}$ and $F_{y\text{R}}^{\text{eq}}$ are functions of the other five variables listed above, Eq. (4) is a system of three equations in five variables that must be determined to define an equilibrium state of the vehicle. Therefore, it is necessary to constrain two of the five variables in order to solve the system of equations. In this analysis, U_x^{eq} and δ^{eq} are set to constant values to enable numerical solution of Eq. (4).

With this choice of constraints, the problem of calculating the equilibria of the vehicle reduces to finding the $F_{x\text{R}}^{\text{eq}}, \beta^{\text{eq}}$, and r^{eq} that satisfy Eq. (4) for specified values of U_x^{eq} and δ^{eq}. For the equilibrium data presented in this section, $U_x^{\text{eq}} = 8\,\text{m/s}$ and several values of δ^{eq} are used in the range $-20\,\text{deg}$ to $20\,\text{deg}$.

The calculated equilibria are presented as a function of steer angle in plots of equilibrium sideslip (Fig. 3), yaw rate (Fig. 4), rear longitudinal force (Fig. 5), total rear tire force magnitude (Fig. 6), and front lateral force (Fig. 7). The analysis reveals two distinct classes of equilibria, grouped according to extent of rear tire saturation. The first group, denoted in Figs. 3–7 by an asterisk (*), are typical cornering equilibria at which the rear tire is not
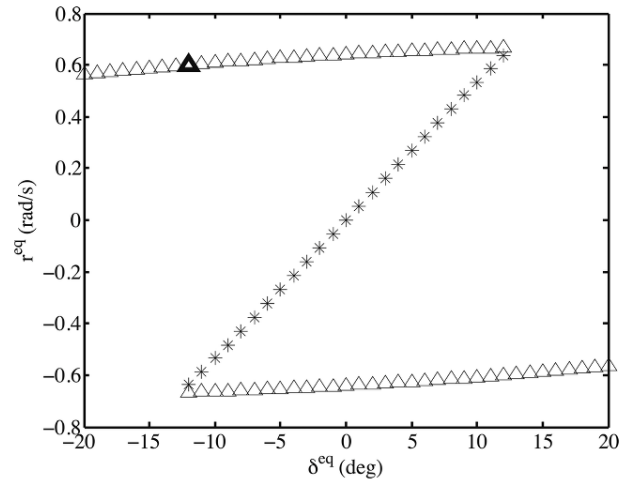

Fig. 6 Magnitude of total rear force versus steer angle, $U_x = 8\,\text{m/s}$. The rear tire friction limit is indicated by a dashed line.

saturated. This is indicated in Fig. 6 by the fact that the rear tire force magnitude at these equilibria lies below the black dashed line representing rear tire friction limit. The second group,

Journal of Dynamic Systems, Measurement, and Control

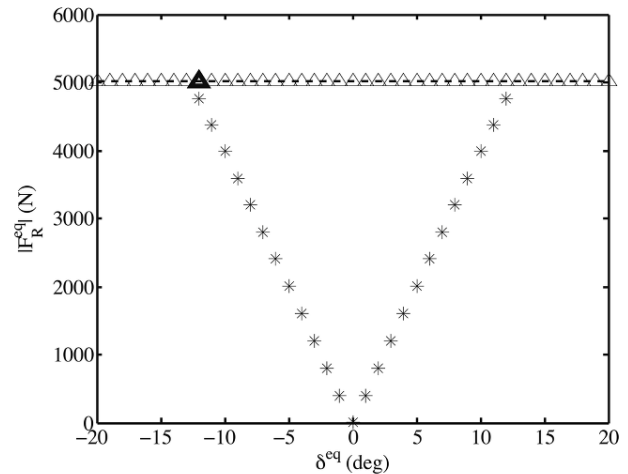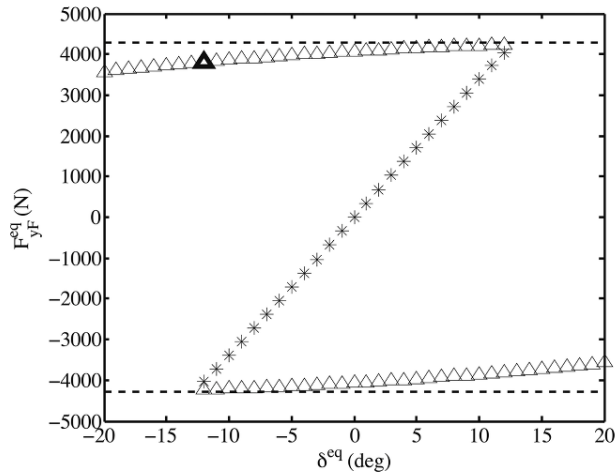**Fig. 7 Equilibrium front lateral force versus steer angle, $U_x = 8$ m/s. The front tire friction limits are indicated by dashed lines.**

denoted in the same figures by triangles (Δ), are drift equilibria at which the rear tire is saturated. This is evident in Fig. 6 from the fact that the rear tire force magnitude at these equilibria lie along the friction limit line. This analysis can also produce a third class of equilibria corresponding to limit understeer (front tire saturation with no rear tire saturation), but the P1 testbed is limit oversteer when operating on the gravel test surface under consideration.

The *-equilibria are typical cornering equilibria because the yaw rate and steer angle have the same sign for these equilibria, and because equilibrium yaw rate increases monotonically with steer angle for these equilibria. Physically, these characteristics signify that the vehicle is turning in the direction that it is steered, and that it turns (yaws) more as it is steered more. At these equilibria, both the front lateral force and total rear tire force are unsaturated. Furthermore, these equilibria are locally stable; many of them represent the steady cornering conditions encountered by average drivers in everyday driving.

The Δ-equilibria have several attributes in addition to rear tire saturation that are characteristics of drifting. The sideslip angle at Δ-equilibria is greater than at the *-equilibria, and quite large in general when the steering angle is also large. Furthermore, Fig. 4 shows that δ^{eq} and r^{eq} have opposite signs at most of the Δ-equilibria, which indicates countersteer.

The rear tire saturation that is characteristic of drift equilibria is also responsible for their open-loop instability. The flow field in Fig. 8, which shows the sideslip and yaw rate state derivatives around a drift equilibrium when $U_x = U_x^{eq} = 8$ m/s, indicates that the equilibrium is an unstable saddle point.

All the characteristics described above can also be observed from the drift equilibria of the two-state model in Ref. [4], but the equilibrium rear longitudinal forces calculated using the three-state model provide additional insights into the role of this input consistent with the higher fidelity models in Refs. [5] and [6]. Figure 5 clearly demonstrates that the amount of longitudinal force required to maintain steady-state drifting is quite large, and is in fact larger than the longitudinal force associated with all of the vehicle's typical cornering equilibria. Furthermore, F_{xR}^{eq} increases monotonically with the magnitude of β^{eq}, meaning that an increase in the rear longitudinal tire force takes the vehicle into a "deeper" drift, at least in steady state.

Not surprisingly, the large drive force at drift equilibria is responsible for the saturation of the rear tire force magnitude observed in Fig. 6. It is this saturation that couples the lateral and longitudinal forces at the rear tire via the friction circle, meaning that F_{yR} is a simple function of the rear drive force input F_{xR} when drifting
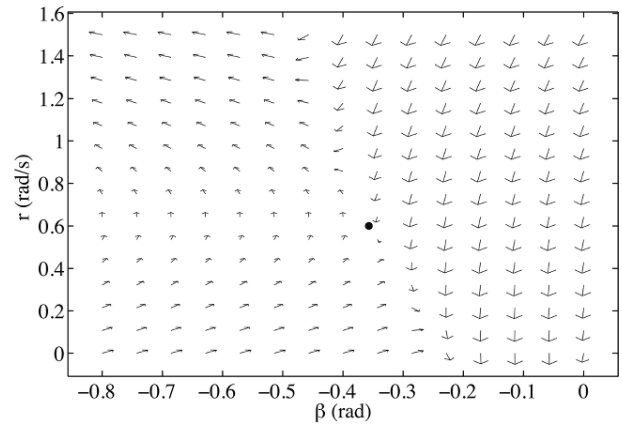

Fig. 8 Flow field of sideslip and yaw rate state derivatives for $U_x = U_x^{eq} = 8$ m/s indicating an open-loop unstable drift equilibrium

$$F_{yR} = \sqrt{(\mu F_{zR})^2 - F_{xR}^2} \tag{5}$$

From a control standpoint, this means that the rear drive force can be used to steer the rear tire in the vicinity of drift equilibria.

The ability to control the rear tire force at drift equilibria is central to the concept of the stability–controllability tradeoff in drifting. This aspect of the equilibria results in an enhanced ability to alter the vehicle trajectory, but at the expense of reduced stability because of the deep rear tire saturation required for drifting. When racing on a dirt or gravel surface where friction is uncertain and varying, however, this enhanced controllability could prove quite valuable in contending with unanticipated vehicle responses. With this in mind, the stability–controllability tradeoff plays a large role in the design of the autonomous drift controller in this work.

4 Control Law

4.1 Control Objective. The primary objective of the drift controller in this work is stabilization to a desired (constant) sideslip angle. A secondary objective of the controller, operating in parallel to the first, is control of the vehicle's longitudinal velocity around a desired value.

The desired sideslip angle and longitudinal velocity are chosen to correspond to one of the equilibria revealed by the preceding analysis. Other aspects of the same equilibrium point are also used in the controller design, in particular the selection of feedforward controller inputs. Thus, while stabilization to a particular equilibrium point is not explicitly a goal of the controller, the equilibrium serves as a useful design guideline, an operating point that can be reached using tractable inputs within the actuator limitations of the testbed.

The drift equilibrium used for controller design is indicated by a bold triangle in Figs. 3–7. The data for this equilibrium are as follows: $\beta^{eq} = -20.44$ deg, $r^{eq} = 0.600$ rad/s, $U_x^{eq} = 8$ m/s, $\delta^{eq} = -12$ deg, $F_{xR}^{eq} = 2293$ N, $F_{yF}^{eq} = 3807$ N, and $F_{yR}^{eq} = 4469$ N.

4.2 Controller Structure and Design. The controller in this work utilizes a variant of the dynamic surface control technique. In particular, it is based on a nested-loop structure wherein yaw rate is treated as a synthetic input to the sideslip dynamics in an outer loop and tire forces are used to feedback linearize the yaw rate dynamics in an inner loop.

This successive loop structure has been chosen (as opposed to direct control of each lateral state) based upon an intuitive examination of the sideslip dynamics of the bicycle model

$$\dot{\beta} = \frac{F_{yF} + F_{yR}}{mU_x} - r \tag{6}$$

The most obvious argument for using yaw rate as a synthetic input to the sideslip dynamics is the appearance of yaw rate as a linear term in these dynamics, as shown in Eq. (6). It is also important to consider that it is difficult to alter the sign or magnitude of the sum $F_{yF} + F_{yR}$ of the lateral forces appreciably when both tires are at or near saturation, as is the case in performance driving. This is especially true relative to the weighted difference $(a/I_z)F_{yF} - (b/I_z)F_{yR}$ that gives the yaw moment acting on the vehicle, where even comparably small changes in the lateral forces relative to one another can be used to effect considerable changes in the magnitude and sign of the yaw moment. Such changes in yaw moment generate large yaw transients that can in turn be used to control the sideslip dynamics.

4.2.1 Outer Loop. The outer loop is designed to control the sideslip dynamics of the vehicle using a desired yaw rate r_{des}. The yaw command in this design utilizes a simple feedforward-feedback structure. The equilibrium yaw rate r^{eq} acts as a feedforward input combined with proportional feedback of the sideslip error $e_\beta = \beta - \beta^{eq}$ relative to the desired equilibrium value

$$r_{des} = r^{eq} + K_\beta e_\beta = \frac{1}{mU_x^{eq}}(F_{yF}^{eq} + F_{yR}^{eq}) + K_\beta e_\beta \qquad (7)$$

where $K_\beta > 0$ is the sideslip error feedback gain.

This command is designed to vary the yaw command in response to sideslip variations from the equilibrium value. For a left-handed drift equilibrium such as the one under consideration in this work ($r^{eq} > 0, \beta^{eq} < 0$), a negative sideslip error ($e_\beta < 0$) signifies that the vehicle is operating at too large of a sideslip angle and is in danger of spinning out. This results in $r_{des} < r^{eq}$, a reduction in the yaw rate command that can be realized through added countersteer, which will in turn prevent a spinout. Conversely, a positive sideslip error ($e_\beta > 0$) signifies that the sideslip angle is too shallow and that the vehicle is in danger of exiting from the drift into a more conventional cornering condition. This results in $r_{des} > r^{eq}$, which can be realized through reduced countersteer and/or reduced rear lateral force (through added rear longitudinal force) to "deepen" the drift as necessary. In either case, the change in the yaw command is appropriate to guide the vehicle sideslip angle back toward the desired value.

4.2.2 Inner Loop. In the inner control loop, the tire lateral forces are chosen in order to feedback linearize the yaw dynamics and enforce stable first-order dynamics in the yaw rate error relative to the outer loop command r_{des}. Defining $e_r = r - r_{des}$, this requirement can be expressed as follows:

$$\dot{e}_r = \dot{r} - \dot{r}_{des} = -K_r e_r \qquad (8)$$

Substituting the yaw dynamics from Eq. (1) for $\dot{r}$ and $\dot{r}_{des} = K_\beta \dot{e}_\beta = K_\beta \dot{\beta}$ yields

$$\dot{e}_r = \frac{aF_{yF} - bF_{yR}}{I_z} - K_\beta \left(\frac{F_{yF} + F_{yR}}{mU_x} - r \right) = -K_r e_r \qquad (9)$$

Rewriting yaw rate as $r = e_r + r_{des}$, substituting for r_{des} from Eq. (7), and collecting like terms yields the following control law:

$$k_1 F_{yF} - k_2 F_{yR} = -K_\beta^2 e_\beta - K_\beta r^{eq} - (K_\beta + K_r)e_r \qquad (10)$$

where $k_1 = (a/I_z) - (K_\beta/mU_x)$ and $k_2 = (b/I_z) + (K_\beta/mU_x)$. It is important to note that this control law does not dictate any individual control input but instead constrains a particular combination of the front tire lateral force F_{yF} and rear tire lateral force F_{yR}. An increase in the controller command (the right-hand side of Eq. (10)), for example, can be achieved by either an increase in F_{yF}, a decrease in F_{yR}, or some combination of the two commands. For this reason, a coordination scheme for the two inputs is required.

4.3 Input Coordination Scheme. The control law as written in Eq. (10) readily permits coordination of inputs assuming that both the front lateral force F_{yF} and rear lateral force F_{yR} can be controlled directly with the available inputs. F_{yF} is of course controlled through the front steer angle. As discussed in Sec. 3, control of F_{yR} exploits rear tire saturation in order to steer the rear tire force using friction circle coupling and the rear drive force F_{xR}.

Coordination of these inputs is built around the concept of the stability–controllability tradeoff. In particular, the inputs are coordinated to maintain steering controllability using the added lateral control authority of the rear longitudinal force as afforded by rear tire saturation. This approach is motivated by an inherent property of drift equilibria. From Fig. 7, the front tire lateral force is very nearly saturated at drift equilibria, indicated by the proximity of the equilibria to the black dashed lines representing the friction limits of the front tire. Consequently, the controller only has a limited ability to increase front lateral force magnitude around drift equilibria before control authority through steering is limited by friction. This limitation in control authority has proven problematic in prior work, since deep front tire saturation led to uncontrolled exits from an autonomous drift in Ref. [4]. With this in mind, it is critical that the front lateral force command does not exceed the front tire force available from friction; the coordination scheme presented below is designed to steer the rear tire using drive force whenever additional cornering force is no longer available at the front tire.

The coordination scheme consists of two controller modes, where the mode of operation is dictated by the amount of cornering force available at the front tire. For the sake of clarity, the derivation of the coordination scheme below focuses upon control of the vehicle about a left-handed drift equilibrium ($r > 0$, $F_{yF} > 0, F_{yR} > 0$). The derivation for a right-handed drift equilibrium is conceptually identical and follows in a similar fashion.

4.3.1 Mode 1: Lateral and Longitudinal Control. In its first mode of operation, the controller attempts to satisfy the drift controller law using steering alone while a longitudinal controller operates in parallel to stabilize the vehicle to a desired longitudinal velocity. The mode 1 longitudinal controller command $^1F_{xR}^{des}$ simply consists of a feedforward term F_{xR}^{eq} and proportional feedback of the longitudinal velocity error $e_{U_x} = U_x - U_x^{eq}$ relative to the longitudinal velocity at the desired drift equilibrium

$$^1F_{xR}^{des} = F_{xR}^{eq} - mK_{U_x}e_{U_x} \qquad (11)$$

The steering command for the drift controller comes from Eq. (10) re-arranged to solve for a front lateral force command

$$^1F_{yF}^{des} = \frac{1}{k_1}[k_2 {}^1F_{yR} - K_\beta^2 e_\beta - K_\beta r^{eq} - (K_\beta + K_r)e_r] \qquad (12)$$

where $^1F_{yR}$ is the computed rear lateral force when operating in mode 1. Note that in mode 1, the rear lateral force is not treated as an input, but rather an additional term in the dynamic surface controller command that is a function of the vehicle state and $^1F_{xR}^{des}$.

$^1F_{yF}^{des}$ can be mapped to a desired front tire slip angle $^1\alpha_F^{des}$ through an inverse Fiala tire model. A steer angle command $^1\delta^{des}$ can then be computed according to Eq. (13), which is a rearrangement of the definition of the front tire slip angle

$$^1\delta^{des} = \arctan \frac{U_y + ar}{U_x} - {}^1\alpha_F^{des} \qquad (13)$$

If $^1F_{yF}^{des} < \mu F_{zF}$, then the drift controller command is satisfied in mode 1, without coordination of steering and longitudinal inputs.

4.3.2 Mode 2: Input Coordination for Lateral Control. In the event that the front lateral force command in mode 1 exceeds the front tire force available from friction ($^1F_{yF}^{des} > \mu F_{zF}$), the drift

controller operates in mode 2. In this mode, both the front and rear tire lateral forces are treated as control inputs to the vehicle, and the rear lateral force command is mapped to a rear longitudinal force via the friction circle

$$^2F_{yR}^{\text{des}} = \frac{1}{k_2}[k_1\mu F_{zF} + K_\beta^2 e_\beta + K_\beta r^{\text{eq}} + (K_\beta + K_r)e_r] \qquad (14)$$

$$^2F_{xR}^{\text{des}} = \sqrt{(\mu F_{zR})^2 - (^2F_{yR}^{\text{des}})^2} \qquad (15)$$

$$^2F_{yF}^{\text{des}} = \mu F_{zF} \qquad (16)$$

$^2F_{yF}^{\text{des}}$ and $^2F_{yR}^{\text{des}}$ are the desired front and rear lateral forces when operating in mode 2, respectively. As in mode 1, the front lateral force command can be mapped to a steering command $^2\delta^{\text{des}}$ using the desired slip angle $^2\alpha_F^{\text{des}}$ and Eq. (13).

In this mode, the front lateral force command (Eq. (16)) is simply set to the maximum achievable value, and the desired rear lateral force (Eq. (14)) is then computed by re-arranging Eq. (10) to solve for rear lateral force assuming $F_{yF} = {}^2F_{yF}^{\text{des}} = \mu F_{zF}$. Since $^2F_{yF}^{\text{des}} < {}^1F_{yF}^{\text{des}}$, it will also be the case that $^2F_{yR}^{\text{des}} < {}^1F_{yR}$.

Knowing that $^2F_{yR}^{\text{des}} < {}^1F_{yR}$, Eq. (15) dictates that $^2F_{xR}^{\text{des}} > {}^1F_{xR}^{\text{des}}$. Thus, the coordination scheme increases the rear drive force as the front tire force saturates. As this scenario is typically encountered when the vehicle's sideslip angle is too shallow, the coordination scheme is using an increase in rear drive force to deepen the vehicle's drift, consistent with the role of rear drive force as observed in the equilibrium analysis.

5 Stability Analysis

The control design presented above is based upon the physical intuition afforded by the analysis of the drift equilibria. However, there is no stability guarantee incorporated in to the design of the controller, and certain aspects of the closed-loop system present interesting challenges from a stability standpoint.

The first of these challenges relates to a distinction between assumptions of the equilibrium analysis in Sec. 3 and the actual behavior of the system when operating in closed-loop. The equilibrium analysis determined steady cornering conditions for the vehicle assuming a fixed front steer angle, whereas the controller continually varies the front steer angle as part of its operation. As a consequence, there is no guarantee that the calculated equilibrium condition guiding the controller's design actually exists for the closed-loop system.

The usage of the rear drive force input for the dual purposes of lateral and longitudinal control represents a challenge as far as enforcing stability of the longitudinal dynamics of the vehicle. While operation of the controller in mode 1 incorporates longitudinal velocity error feedback into the rear drive force input, mode 2 uses the rear drive force exclusively for the purpose of lateral control. In the latter case, the controller temporarily sacrifices control of the longitudinal velocity error e_{U_x} for the sake of control in the $e_\beta - e_r$ plane. As discussed in Sec. 4.3, operation in mode 2 results in a larger rear drive force input than in mode 1. While it is clear that this will induce positive longitudinal velocity errors, it is unclear how the added energy input to the system will affect overall longitudinal stability in closed-loop.

The analysis that follows demonstrates that these potential stability issues are not problematic in a neighborhood around the equilibrium used for control design by establishing the existence of an invariant set around this equilibrium. The invariant set has been generated by expressing the closed-loop dynamics of the vehicle in a form that facilitates the usage of simple Lyapunov techniques to compute an invariant set.

5.1 Closed-Loop Dynamics. The closed-loop dynamics of the vehicle can be written in terms of the state vector

$e = [e_\beta \ e_r \ e_{U_x}]^T$ by grouping the linear components of the closed-loop dynamics together and treating the remaining nonlinear dynamics as an additional disturbance vector

$$\begin{bmatrix} \dot{e}_\beta \\ \dot{e}_r \\ \dot{e}_{U_x} \end{bmatrix} = \begin{bmatrix} -K_\beta & -1 & 0 \\ 0 & -K_r & 0 \\ \frac{\partial f_x}{\partial e_\beta} & \frac{\partial f_x}{\partial e_r} & \frac{\partial f_x}{\partial e_{U_x}} \end{bmatrix}\Bigg|_{e^{\text{eq}},\delta^{\text{eq}}} \begin{bmatrix} e_\beta \\ e_r \\ e_{U_x} \end{bmatrix} + \begin{bmatrix} \Delta_\beta \\ 0 \\ \Delta_{U_x} \end{bmatrix} \qquad (17)$$

The closed-loop sideslip and yaw dynamics as written above can be derived directly from the governing equations for sideslip and yaw in the bicycle model (Eq. (1)) when operating in closed-loop. The longitudinal dynamics as written above are based upon a linear approximation in the neighborhood of the equilibrium as obtained from the gradient of the function f_x in Eq. (18) evaluated at $e^{\text{eq}} = [0\ 0\ 0]^T$ and $\delta = \delta^{\text{eq}}$

$$f_x = -K_{U_x}e_{U_x} + \frac{1}{m}(F_{xR}^{\text{eq}} - F_{yF}\sin\delta^{\text{eq}}) + rU_x\beta$$

$$\dot{e}_{U_x} \approx \left[\frac{\partial f_x}{\partial e_\beta} \ \frac{\partial f_x}{\partial e_r} \ \frac{\partial f_x}{\partial e_{U_x}}\right]\Bigg|_{e^{\text{eq}},\delta^{\text{eq}}} \begin{bmatrix} e_\beta \\ e_r \\ e_{U_x} \end{bmatrix} = \nabla f_x(e^{\text{eq}}, \delta^{\text{eq}})e \qquad (18)$$

Note that f_x is just a simplification of the closed-loop longitudinal dynamics in mode 1 with $\sin\delta = \sin\delta^{\text{eq}}$, since δ is a complex function of the states in closed-loop.

5.2 Computation of Invariant Set. The existence of an invariant set is demonstrated in this work by finding a Lyapunov function for the system of the form $V(e) = e^T P e$ ($P \succ 0$) where it is possible to find a level curve $V(e) = c$ (c a constant) such that $\dot{V}(e) \leq 0$ whenever $V(e) \leq c$ (an invariant set). The challenge lies in finding a Lyapunov function for which this condition actually holds.

In this work, a candidate Lyapunov function is generated by solving the continuous-time Lyapunov equation for P

$$A^{\text{CL}^T}P + PA^{\text{CL}} = -I \qquad (19)$$

The matrix A^{CL} is taken directly from the closed-loop dynamics of the system as given in Eq. (17) and reflects the linear component of these dynamics

$$A^{\text{CL}} = \begin{bmatrix} -K_\beta & -1 & 0 \\ 0 & -K_r & 0 \\ \frac{\partial f_x}{\partial e_\beta} & \frac{\partial f_x}{\partial e_r} & \frac{\partial f_x}{\partial e_{U_x}} \end{bmatrix}\Bigg|_{e^{\text{eq}},\delta^{\text{eq}}} \qquad (20)$$

Solution of the Lyapunov equation results in a matrix P that enforces $\dot{V}(e) = -e^T e$ for the linear system $\dot{e} = A^{\text{CL}}e$. However, as shown in Eq. (17), the closed-loop dynamics of the vehicle are actually of the form $\dot{e} = A^{\text{CL}}e + \Delta$, where Δ represents additional nonlinearities in the dynamics. Consequently, the matrix P computed in this manner only represents a candidate Lyapunov function for the actual closed-loop dynamics. The ability of this function to actually yield an invariant set must be tested numerically, as detailed below.

With $K_\beta = 2, K_r = 4, K_{U_x} = 0.423$ and the drift equilibrium given earlier as the control objective, solving Eq. (19) gives the P below

$$P = \begin{bmatrix} 4.680 & 1.032 & 0.436 \\ 1.032 & 8.294 & 0.212 \\ 0.436 & 0.212 & 0.241 \end{bmatrix} \qquad (21)$$
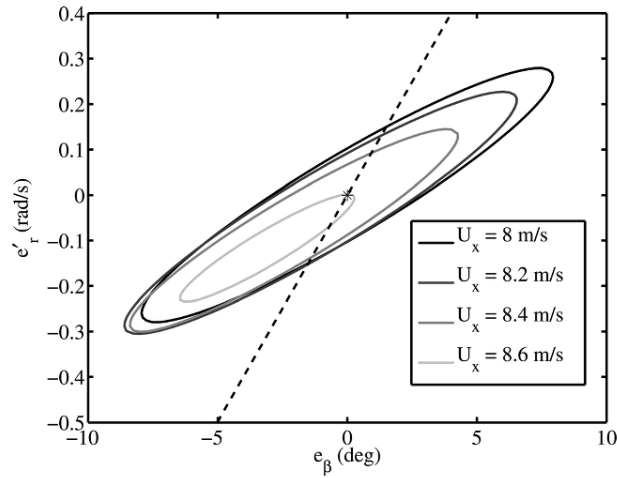
Fig. 9 2D sections of invariant set, U_x = 8–8.6 m/s. The eigenvector corresponding to the stable eigenvalue of the open-loop linearization is shown with a dashed line.
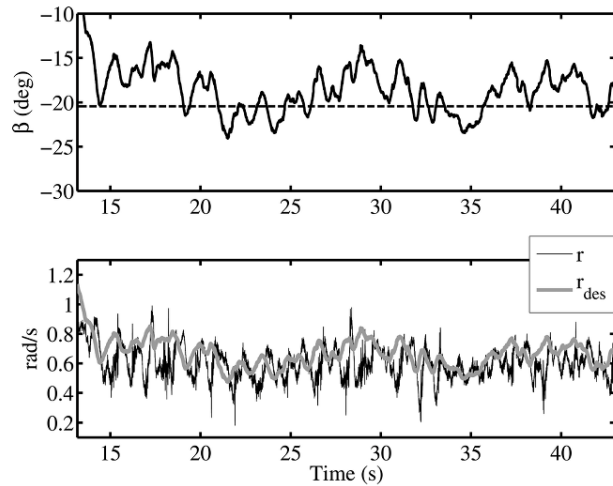

Fig. 10 Sideslip compared to β^{eq} (top) and yaw rate compared to r_{des} (bottom) during experimental run

P can be tested numerically by computing $\dot{V}(e) = \dot{e}^T P e + e^T P \dot{e}$ in a neighborhood of $e = 0$. The time derivative of the states $\dot{e} = \begin{bmatrix} \dot{e}_\beta & \dot{e}_r & \dot{e}_{U_x} \end{bmatrix}^T$ is computed using the closed-loop dynamics of the bicycle model, accounting for all nonlinearities, tire force limitations due to friction, and steering angle limits

$$\dot{e}_\beta = \dot{\beta} = \frac{1}{mU_x}(F_{yF}^{CL} + F_{yR}^{CL}) - r$$

$$\dot{e}_r = \dot{r} - K_\beta \dot{e}_\beta = \left(\frac{a}{I_z} - \frac{K_\beta}{mU_x}\right)F_{yF}^{CL} - \left(\frac{b}{I_z} + \frac{K_\beta}{mU_x}\right)F_{yR}^{CL} - K_\beta r$$

$$\dot{e}_{U_x} = \dot{U}_x = \frac{1}{m}(F_{xR}^{CL} - F_{yF}^{CL}\sin\delta^{CL}) + rU_x\beta \qquad (22)$$

where $F_{yF}^{CL}, F_{yR}^{CL}, F_{xR}^{CL}$, and δ^{CL} are the values of the tire forces and steer angle as calculated when operating in closed-loop.

This numerical analysis reveals that the set $V(e) = e^T P e \leq 0.0875$ defines an invariant set around $e = 0$, demonstrating local stability of the system. This particular level curve $V(e)$ was manually selected by finding as large an invariant set for the system as possible while ensuring that the conditions for an invariant set given earlier are satisfied.

A straightforward physical interpretation of this invariant set is made possible by visualizing the set in a slightly different coordinate system where yaw error is defined with respect to the (fixed) equilibrium yaw rate r^{eq} instead of $r_{des} = r^{eq} + K_\beta e_\beta$, which is both time-varying and coupled with e_β. The yaw error e_r' in this alternate coordinate system is defined in terms of e_r as follows:

$$e_r' = r - r^{eq} = e_r + K_\beta e_\beta \qquad (23)$$

Using Eq. (23), the coordinate systems (e_β, e_r, e_{U_x}) and (e_β, e_r', e_{U_x}) can be related by a simple linear transformation. This linear transformation can be used to map the invariant set as calculated in the (e_β, e_r, e_{U_x}) space to the corresponding invariant set in the (e_β, e_r', e_{U_x}) space.

Figure 9 gives two-dimensional sections of the level curve corresponding to $V(e) = 0.0875$ in the $e_\beta - e_r'$ plane for a range of longitudinal velocities. The area contained within each of the sections gives the set of initial conditions in the invariant set at the corresponding longitudinal velocity. When operating at or near the equilibrium velocity of 8 m/s, the controller provides stabilization over a wide range of sideslip and yaw rate errors. As longitudinal velocity increases above the equilibrium value ($e_{U_x} > 0$), however, the invariant set decreases considerably in size and shifts away from positive sideslip errors ($e_\beta > 0$). This is most evident in Fig. 9 from the section of the invariant set through $U_x = 8.6$ m/s.

The observed shift in the invariant set for $e_{U_x} > 0$ can be viewed as a consequence of using the rear longitudinal force for both lateral and longitudinal control. This is because the lateral and longitudinal control objectives for the rear longitudinal force can be at odds with one another when both $e_{U_x} > 0$ and $e_\beta > 0$. To be specific, longitudinal control when $e_{U_x} > 0$ requires a reduction in rear longitudinal force, whereas $e_\beta > 0$ (signifying that the vehicle is exiting the drift) may require lateral control in mode 2 and a subsequent increase in rear longitudinal force. If the magnitudes of the sideslip and longitudinal velocity errors in this scenario are large enough, it may no longer be possible to maintain stability of the longitudinal dynamics while also satisfying the lateral control objective in mode 2.

The yaw characteristics of the invariant set are consistent with physical intuition on the role of yaw rate in the sideslip dynamics when drifting. The invariant set is oriented diagonally in the $e_\beta - e_r'$ plane from a region of negative sideslip and yaw rate errors at one extreme to positive sideslip and yaw rate errors at the other. In the former region, the sideslip magnitude is too large, but a low yaw rate relative to r^{eq} (as would result from countersteer) acts through the sideslip dynamics to reduce the sideslip magnitude back toward equilibrium. In the latter region, the sideslip magnitude is too low, but a high yaw rate relative to r^{eq} (as would result from reduced rear lateral force via added drive force) acts through the sideslip dynamics to increase the sideslip angle back toward equilibrium.

Finally, there is a rather interesting connection between the invariant set for the system in closed-loop and the open-loop stability characteristics of the drift equilibrium. Since the drift equilibrium is a saddle node in open-loop, some state trajectories closely approach the equilibrium before diverging, as is evident from the flow field in Fig. 8. These trajectories lie near the eigenvector corresponding to the stable eigenvalue of the open-loop linearization of the system. The invariant set for the closed-loop system is oriented such that it roughly coincides with these "favorable" state trajectories, as indicated by the dashed line in Fig. 9 that gives the orientation of the eigenvector for the stable eigenvalue. This is not surprising, as the controller should be most effective where its action complements the natural dynamics of the system.

6 Experimental Investigation

The controller has been implemented on P1, a RWD by-wire testbed built by students at Stanford University (Fig. 2). P1's
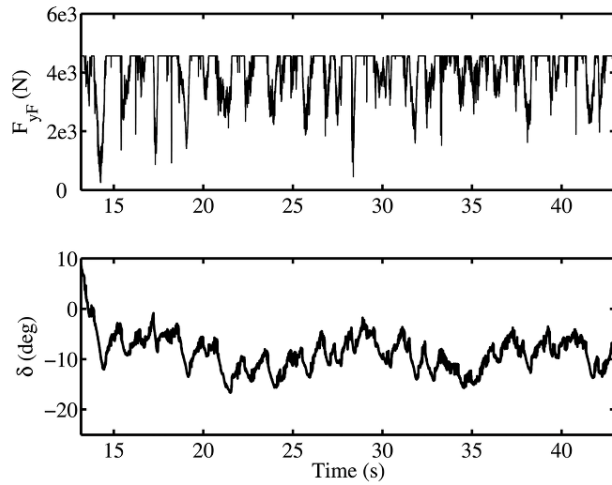
Fig. 11 Front lateral force command (top) and steering command (bottom) during experimental run

Fig. 12 Longitudinal velocity (top) and rear drive force command (bottom) during experimental run

steer-by-wire system generates the steering commands computed by the controller, while a drive-by-wire system issues torque commands to the vehicle's drive motors using an open-loop torque map. The torque commands to the drive motors are determined using Eq. (24) to compute the rear torque command τ_R^{des} corresponding to a rear longitudinal force command F_{xR}^{des}

$$\tau_R^{des} = \frac{F_{xR}^{des} r_w}{k_{gr}} \tag{24}$$

where r_w is the effective rear wheel radius and k_{gr} is the transmission gear ratio. This approach to calculating drive torques neglects delays due to drivetrain and wheelspeed dynamics; these dynamics are fast relative to the overall vehicle dynamics because they are dictated primarily by the small inertias of the rear wheels and other drivetrain components.

Since the primary focus of this work is a fundamental investigation of drifting rather than the development of algorithms for a production setting, the controller utilizes estimates of sideslip, yaw rate, and longitudinal velocity obtained from fusion of global positioning system (GPS) and inertial navigation system (INS) sensor measurements using techniques developed in Ref. [11]. Under more practical circumstances, however, the controller could be implemented in concert with the estimator detailed in Ref. [12] that provides estimates of sideslip and friction from measurements of steering torque. This estimator has been used successfully for vehicle control under high-sideslip conditions in Ref. [13] and would enable operation without an extensive sensor set or an a priori estimate of the surface friction coefficient.

Experimental runs take place at a gravel lot where the friction coefficient $\mu \approx 0.55$ but is subject to significant variability because of nonuniformity of the testing surface. Each experimental run begins with an open-loop control sequence in which the vehicle is brought up to speed and then destabilized. The controller is then activated and used to initiate the drift. The equilibrium condition given in Sec. 4.1 and controller parameters $K_\beta = 2$, $K_r = 4$, and $K_{U_x} = 0.846$ are used to obtain the experimental results that follow.

6.1 Experimental Results. During the experimental run depicted in Figs. 10–12, the vehicle successfully drifts autonomously for more than 30 s before the experimental run is deliberately ended by a "safety driver" seated in the testbed and monitoring the controller. From the top plot in Fig. 10, it is evident that the measured sideslip angle tracks the target sideslip (denoted by a dashed line) quite closely, with sideslip error rarely exceeding 3–5 deg in magnitude. In fact, the sideslip angle
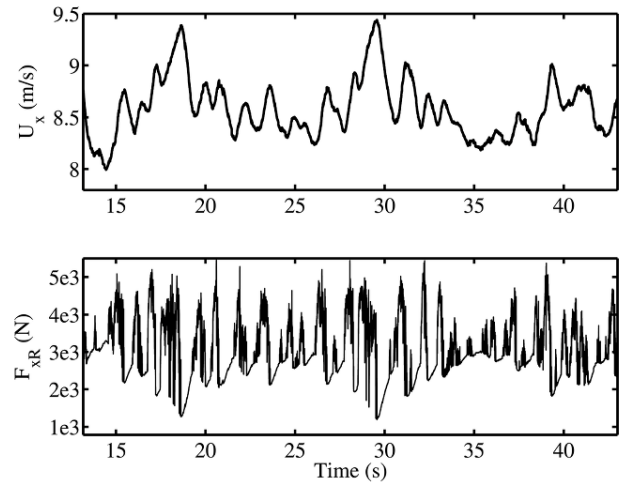
remains within a range comparable to or better than that achieved by a human driver in measurements of drifting from Ref. [6].

It is important to remember that friction on the test surface is highly variable, and the larger sideslip deviations are due in large part to friction disturbances acting through the yaw dynamics. The successive loop structure of the controller makes sideslip tracking performance contingent upon the ability of the inner yaw control loop to track the yaw command from the outer loop. Consequently, large yaw errors will eventually translate to large sideslip errors. It is no coincidence, then, that sideslip excursions such as the one observed at $t = 31$ s are preceded by large drops in yaw rate (bottom plot of Fig. 10) caused by increases in friction on the surface. These yaw drops result in large negative yaw errors, and act through the sideslip dynamics to decrease sideslip magnitude.

Fortunately, the input coordination incorporated into the controller design proves highly effective in anticipating and contending with decreases in sideslip magnitude. The controller responds to precipitous drops in yaw rate such as the one at $t = 31$ s by commanding a rapid increase in the yaw command r_{des}. This, in turn, causes a transition from mode 1 of controller operation to mode 2. Front countersteer is reduced as the front lateral force command is saturated to the front tire friction limit (top plot of Fig. 11), and the rear drive force command (bottom plot of Fig. 12) rapidly climbs to reduce the rear lateral force magnitude. These control responses drive the vehicle yaw rate up toward r_{des}, and this yaw buildup then acts through the sideslip dynamics to increase sideslip magnitude.

In general, the controller provides stabilization over a considerably larger region of the state space than predicted by the stability analysis. As discussed above, the controller recovers from rather significant aberrations in yaw and sideslip tracking. Furthermore, the controller operates over a fairly broad longitudinal velocity range in experiments (top plot of Fig. 12), with speed tracking errors induced by using the rear drive force for lateral control proving to be less problematic than predicted by the analysis. This result is made more impressive by the fact that this experimental performance is achieved under rather challenging test conditions. The controller performs robustly in spite of the use of an approximate open-loop map for rear longitudinal force control and the presence of disturbances due to considerable friction variation.

7 Conclusion

Beginning with a three-state model that achieves a balance between model fidelity and simplicity for the purposes of control design, this work has presented the design, stability verification, and experimental validation of a controller for autonomous

drifting of a RWD vehicle. This development process was rooted in a fundamental observation about the nature of drifting revealed through analysis of the three-state model: Drifting represents a tradeoff of vehicle stability for added controllability. This tradeoff results from the fact that the rear tire saturation inherent to drifting reduces vehicle stability, but enables steering of the rear tire using drive force because its lateral and longitudinal forces are coupled through a simple mathematical relationship at saturation.

This insight is reflected directly in a novel characteristic of the autonomous drift controller design, which leverages the rear drive force input for lateral control whenever controllability via the front lateral force is friction-limited. From a control perspective, this results in a unique challenge, as the rear drive force must be used for longitudinal and lateral control. Nonetheless, the controller achieves closed-loop stabilization in reasonably large neighborhood around a target drift equilibrium. This was demonstrated analytically, through a stability analysis, but more importantly through robust experimental performance under challenging test conditions that included significant friction variability.

The controller's impressive robustness in experiments, with its ability to provide stabilization over a larger region of the state space than predicted by the stability analysis, warrants further investigation in future work. In particular, the usage of the rear longitudinal force for both longitudinal and lateral control has proven less problematic than the stability analysis would suggest; the controller is able to recover from fairly significant longitudinal velocity errors induced by modulation of the rear longitudinal force for lateral control. A more explicit understanding of the mechanisms in the closed-loop dynamics that enable such robust stability characteristics can lead to new controllers and input coordination techniques that explicitly account for these mechanisms in their design. In this fashion, it may be possible to improve controller performance while also facilitating an analytical demonstration of the controller's robustness.

From a broader perspective, the controller's successful performance in the presence of high friction variability lends credence to the notion of cornering with deliberate rear tire saturation as a robust approach to vehicle trajectory control in uncertain conditions. The autonomous drift controller in this work can be viewed as a proof-of-concept for this approach, for harnessing the advantageous aspects of high-sideslip dynamics and rear tire saturation rather than avoiding these dynamics entirely. With this in mind, continued efforts to better understand the dynamics of vehicles with rear tire saturation could lead to a new class of safety systems that reflect this perspective and enable more flexible control of vehicle trajectory at and beyond the handling limits, under a wide range of operating conditions.

References

[1] Velenis, E., and Tsiotras, P., 2005, "Minimum Time vs Maximum Exit Velocity Path Optimization During Cornering," ISIE 2005, Croatia, Dubrovnik, June 20–23, Vol. 1, pp. 355–360.

[2] Velenis, E., Tsiotras, P., and Lu, J., 2008, "Optimality Properties and Driver Input Parameterization for Trail-Braking Cornering," Eur. J. Control, 14(4), pp. 308–320.

[3] Ono, E., Hosoe, S., and Tuan, H., 1998, "Bifurcation in Vehicle Dynamics and Robust Front Wheel Steering Control," IEEE Trans. Control Syst. Technol., 6(3), pp. 412–420.

[4] Voser, C., Hindiyeh, R., and Gerdes, J., 2010, "Analysis and Control of High Sideslip Manoeuvres," Veh. Syst. Dyn., 48, pp. 317–336.

[5] Edelmann, J., Plochl, M., Lugner, P., Mack, W., and Falkner, A., 2008, "Investigations on the Powerslide of Automobiles," AVEC 2008, Kobe, Japan, Oct. 6–9.

[6] Velenis, E., Katzourakis, D., Frazzoli, E., Tsiotras, P., and Happee, R., 2010, "Stabilization of Steady-State Drifting for a RWD Vehicle," AVEC 2010, Loughborough, UK, Aug. 22–26.

[7] Abdulrahim, M., 2006, "On the Dynamics of Automobile Drifting," SAE World Congress 2006, Detroit, MI, April 3-6, Paper No. 2006-01-1019.

[8] Edelmann, J., Plochl, M., and Pfeffer, P., 2011, "Analysis of Steady-State Vehicle Handling and Driver Behaviour at Extreme Driving Conditions," IAVSD 2011, Manchester, UK, August 14–19.

[9] Velenis, E., Frazzoli, E., and Tsiotras, P., 2010, "Steady-State Cornering Equilibria and Stabilization for a Vehicle During Extreme Operating Conditions," Int. J. Veh. Auton. Syst., 8(2–4), pp. 217–241.

[10] Fiala, E., 1954, "Seitenkrafte am Rollenden Luftreifen," VDI Z., 96(29), pp. 973–979.

[11] Ryu, J., and Gerdes, J., 2004, "Integrating Inertial Sensors With GPS for Vehicle Dynamics Control," ASME J. Dyn. Syst., Meas., Control, 126(2), pp. 243–254.

[12] Hsu, Y.-H., Laws, S., and Gerdes, J., 2010, "Estimation of Tire Slip Angle and Friction Limits Using Steering Torque," IEEE Trans. Control Syst. Technol., 18(4), pp. 896–907.

[13] Beal, C. E., 2011, "Applications of Model Predictive Control to Vehicle Dynamics for Active Safety and Stability," Ph.D. thesis, Stanford University, Stanford, CA.